Journal of Applied Polymer Science

In situ polymerization of polyimide-based nanocomposites via covalent incorporation of functionalized graphene nanosheets for enhancing mechanical, thermal, and electrical properties

Yong Qian, Hongfu Wu, Dingzhong Yuan, Xing Li, Wenting Yu, Chunyan Wang
Fundamental Science on Radioactive Geology and Exploration Technology Laboratory, Department of Materials Science and Engineering, East China Institute of Technology, Nanchang, Jiangxi 330013, China
Correspondence to: Y. Qian (E-mail: yqianecit@163.com)

ABSTRACT: In this study, we report an effective method to fabricate high-performance polyimide (PI)-based nanocomposites using 3-aminopropyltriethoxysilane functionalized graphene oxide (APTSi-GO) as the reinforcing filler. APTSi-GO nanosheets exhibit good dispersibility and compatibility with the polymer matrix because of the strong interfacial covalent interactions. PI-based nanocomposites with different loadings of functionalized graphene nanosheets (FGNS) were prepared by *in situ* polymerization and thermal imidization. The mechanical performance, thermal stability, and electrical conductivity of the FGNS/PI nanocomposites are significantly improved compared with those of pure PI by adding only a small amount of FGNS. For example, a 79% improvement in the tensile strength and a 132% increase in the tensile modulus are achieved by adding 1.5 wt % FGNS. The electrical and thermal conductivities of 1.5 wt % FGNS/PI are 2.6×10^{-3} S/m and 0.321 W/m·K, respectively, which are $\sim 10^{10}$ and two times higher than those of pure PI. Furthermore, the incorporation of graphene significantly improves the glass-transition temperature and thermal stability. The success of this approach provides a good rationale for developing multifunctional and high-performance PI-based composite materials. © 2015 Wiley Periodicals, Inc. J. Appl. Polym. Sci. **2015**, *132*, 42724.

KEYWORDS: composites; films; mechanical properties; polyimides

Received 15 April 2015; accepted 12 July 2015
DOI: 10.1002/app.42724

INTRODUCTION

Polymer composites are made by compounding of reinforcing filler with polymer matrix. The incorporation of filler generally enhanced overall properties of polymer matrix, and thus they have widely used in various fields of application, such as sport goods, construction, automotive, marine, and aerospace. Up to now, different fillers such as carbon black (CB),[1] carbon nanofiber (CF),[2] rice bran carbon,[3] carbon nanotube (CNT),[4,5] nanoclay,[6] fullerene,[7] diamond nanoparticles,[8] and starch[9,10] have been used extensively for improving the thermal, mechanical, electrical, gas barrier, and abrasion resistance properties of composites.

Carbon nanocomposites with a polymer matrix are believed to be a new breakthrough in materials science.[11] Graphene, a single-atom-thick sheet of hexagonally arrayed sp^2-bonded carbon atoms, is considered as the most promising carbon material in the future, since it was successfully exfoliated in 2004.[12] Owing to the fascinating physical properties and unique structure, graphene exhibits excellent performance such as outstanding mechanical strength (Young's modulus of 1 TPa and ultimate strength of 130 GPa),[13] superior electrical conductivity (up to 6000 S/cm),[14] extremely high surface area (theoretical limit: 2630 m^2/g),[15] high thermal conductivity (5000 W/m·K),[16] and thermal stability. Because of the fascinating properties, graphene has great potential in various applications such as field-effect transistors,[17] lithium-ion batteries,[18] drug delivery and cell imaging,[19,20] chemical and biosensors,[21] supercapacitors,[22] toxic material removal,[23] solar cells,[24] and particularly as the reinforcement to develop high-performance multifunctional polymer nanocomposites. Recently, several studies have focused on graphene-based polymer composites to achieve those unique properties such as mechanical strength and modulus, thermal stability, and electrical conductivity,[11,25,26] which rely on the dispersion of graphene in polymer matrices.[15,26,27] A well-dispersed state maximizes the reinforced surface area, thereby enhancing the properties of nearby polymer chains and entire matrix. However, pristine graphene sheets, hydrophobic in nature, have

Additional Supporting Information may be found in the online version of this article.

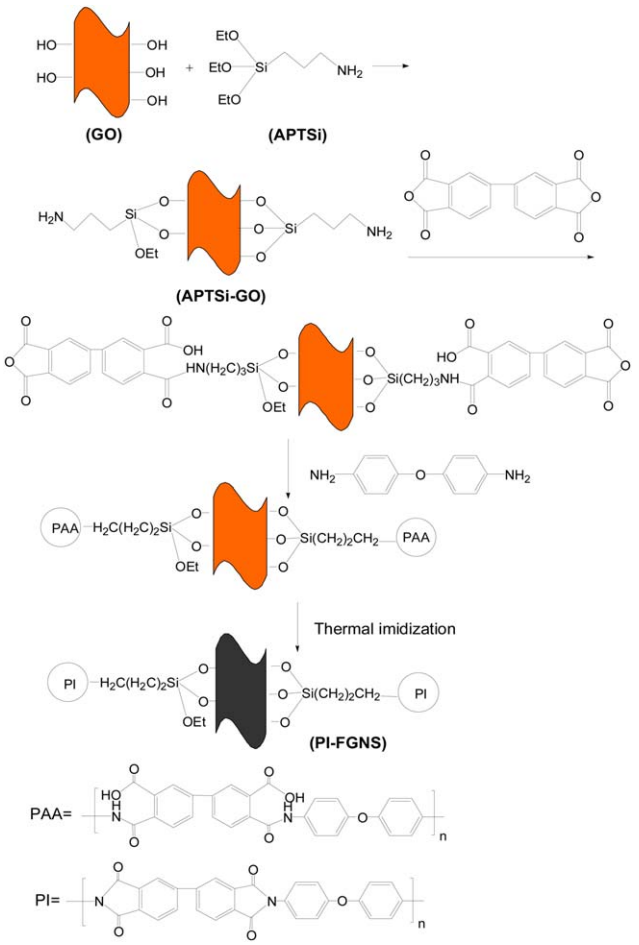

Scheme 1. Schematic diagram for the preparation of APTSi-GO and FGNS-incorporated PI composites (FGNS/PI). [Color figure can be viewed in the online issue, which is available at wileyonlinelibrary.com.]

a distinct tendency to agglomerate or restack irreversibly in composites because of the strong π–π stacking interactions between the layers and incompatible surface characteristics with the polymer matrices. Therefore, the proper dispersion of graphene in a polymer matrix is still challenging.[28,29] To overcome this problem, several efforts have been focused on achieving a uniformly dispersed system by noncovalent or covalent functionalization of graphene surface. Nowadays, most of the strategies involve graphene oxide (GO) as the starting material, whose hydrophilic nature makes it highly dispersible in aqueous media as individual sheets. Therefore, the noncovalent functionalization of GO with different organic compounds has been carried out, including isocyanate modification,[30,31] long alkyl chains[32,33] and long-chain alkyl silane functionalization,[34] and ionic liquid modification.[35] Compared with noncovalent modification, covalent modification provides stronger interfacial interactions between the nanofiller and polymer matrix. Covalent modifications such as amination,[36,37] esterification,[38] diazonium functionalization, silane modification,[39] and polymer grafting[40] are critical in improving the synergistic dispersion effect of graphene nanohybrids.

Polyimides (PIs) are an important class of structural polymers with excellent physicochemical properties such as thermal and thermo-oxidative stability, superior mechanical and dielectrical properties, and favorable chemical and solvent resistance properties. Therefore, they are widely used in the microelectronics and aerospace industries.[41,42] However, pure PI with insulating nature has a few limitations such as electrostatic accumulation, poor heat dissipation, and low electrical conductivity for particular applications.[43] Recently, carbon nanomaterial has been used to improve the properties of PI materials. For CNT/PI composites, functionalized CNTs have been demonstrated as effective nanofillers to improve their mechanical, electrical, and thermal properties.[44,45] Although various surface functionalization and polymer grafting methods have been used for exfoliating CNT bundles, it is still difficult to achieve high-performance composites in which CNTs are individually dispersed in polymer matrix because of the strong entanglement of CNTs. In this context, graphene has been used as nanofillers to reinforce the properties of PI, which has set up a new avenue for the synthesis of high-performance PI-based composites.[46–48]

Herein, we report a novel strategy to build strong interfaces between functionalized graphene nanosheets (FGNS) and PI matrix for high high-performance FGNS/PI composites. The amino-functionalized GO, which was synthesized using 3-aminopropyltriethoxysilane (APTSi), was utilized as the reinforced filler to form strong intrachain covalent bonds with polyamic acid (PAA, the precursor of PI). After the imidization, the as-obtained FGNS/PI composites exhibited better mechanical properties, thermal stability, and electrical and thermal conductivities than pure PI. The reinforcement mechanism was discussed based on the investigation on the covalent bonding compatibility and dispersity of the composites.

EXPERIMENTAL

Materials

3,3′,4,4′-Biphenyl tetracarboxylic dianhydride (BPDA) and 4,4'-Diaminodiphenyl ether (ODA) (Shanghai Guchuang Chem. Co.) were purified by sublimation. N, N-dimethylacetamide (DMAc) (Shanghai Haoshen Chem. Co.) was distilled over CaH_2 under reduced pressure prior to use. 3-aminopropyltriethoxysilane (APTSi, 99%) was obtained from Aldrich. Potassium permanganate ($KMnO_4$), sodium nitrate ($NaNO_3$), 98% sulfuric acid (H_2SO_4), 37% hydrochloric acid (HCl), 30% hydrogen peroxide (H_2O_2), and natural graphite powder (300 mesh) were commercially purchased from China Medicine Co. All reactants were analytical purity.

Preparation of APTSi Functionalization of GO Sheets (APTSi-GO)

The graphene oxide (GO) was synthesized from natural graphite powder according to the literature, as reported in detail elsewhere.[49] The process has been described in our previous study.[50] As-purified GO powders were distributed in DMAc to create a homogenous yellow-brown dispersion (1 mg/mL) ready for use. The surface of GO was modified using APTSi, as shown in Scheme 1. In a typical experiment, 100 mg of GO was homogeneously dispersed in 100 mL of DMAc by ultrasonication at room temperature. Next, 0.2 mL triethylamine and 1 g APTSi

were slowly added into a 500 mL round-bottomed flask with stirring for 24 h at 100°C under nitrogen. The reaction mixture was filtered and washed with anhydrous ethanol in order to remove residual APTSi and then repeatedly washed with deionized water to obtain neutral product and dried in a vacuum at 60°C. A total of 1.0 mg/mL APTSi-GO colloid was achieved by dispersing the solid products in DMAc.

Preparation of FGNS/PI Composite Films

A typical procedure for the preparation of the FGNS/PI includes three steps, that is, surface modification of GO with APTSi, *in situ* polymerization, and thermal imidization, as shown in Scheme 1. A 0.1 mol (2.943 g) BPDA was put into a 500 mL three-neck flask containing 100 mL of dry DMAc at 0°C in ice water mixture. After stirring continuously for 3 h under nitrogen gas atmosphere, a certain amount of APTSi-GO, that is, 0.3, 0.5, 1, and 1.5 wt % of PI was introduced into the flask under mechanical stirring for 12 h. Next, 0.1 mol (2.003 g) ODA was added to the above mixed solution with vigorous stirring for 48 h at around 0°C to form a homogeneous, viscous and light yellow polyamic acid (PAA, the precursor of PI) solution. The as-obtained PAA and APTSi-GO/PAA were spread onto a glass plate, and then dried at 70°C for 5 h to remove the residual solvent. Finally, the PI-based films were thermally imidized at 150, 200, 250, and 300°C each for 1 h, and 350°C for 0.5 h under vacuum. During the thermal imidization process, the FGNS/PI films were collected from the glass plates after soaking in water at room temperature for a couple of days.

Measurements

Transmission electron microscopy (TEM) images were obtained from JEM-2100 (Japan) with a 200 kV accelerating voltage. The TEM samples were prepared by drying a droplet of the suspensions on a Cu grid. Atomic force micrographs (AFM) were recorded at an Agilent 5500 AFM/SPM system with Picoscan v 5.3.3 software in tapping mode with samples prepared by spin-coating sample solutions onto freshly exfoliated mica substrates at 1000 rpm under ambient conditions. The structure of the samples was examined by X-ray powder diffractometer (XRD, Shimadzu, X-6000, Cu Kα radiation); X-ray photoelectron spectroscopy (XPS, Kα) analyses were carried out on a Thermo Fisher X-ray photoelectron spectrometer system equipped with Al radiation as a probe, with a chamber pressure of 5×10^{-9} Torr. The source power was set at 72 W, and pass energies of 200 eV for survey scans and 50 eV for high-resolution scans were used. The analysis spot size was 400 μm in diameter.

The mechanical properties were measured by using SANS CMT-8102 stretching tester at a speed of 5 mm/min using thin films of about 5–10 μm thickness. At least five specimens were used for each sample in the tensile test. Thermogravimetric analysis (TGA) was analyzed under an N_2 atmosphere at a heating rate of 10°C/min (Q50; TA Instrument). Dynamic mechanical analysis (DMA) measurements were made using a Netzsch DMA242 analyzer at a heating rate of 5°C/min from 35 to 350°C and a frequency of 1 Hz. Electrical conductivities higher than 10^{-6} S/m were measured using a Keithley 4200-SCS apparatus; below 10^{-6} S/m were tested using a ZC-36 high-resistance meter. The thermal diffusivity (D) of the PI-based composite thin films was determined using an Ulvac LaserPIT thermal diffusivity meter operated at 25°C in a vacuum. The thin film size was about 30 mm × 5 mm × 0.5 mm and the density (ρ) was calculated by measuring sample dimensions and mass. Specific heat (Cp) was measured by modulated DSC (TA Instruments Q1000). The thermal conductivity (T_c) was calculated from the thermal diffusivity as follows: $T_c = \rho CpD$.[51] The water uptake was measured by putting the samples in a sealed container at 30°C at a relative humidity of 100%. Before the measurement, the samples were dried at 100°C for 24 h in vacuo to remove ant moisture. The water sorption of the sample is achieved as below: S % = 100% $(W_t - W_0)/W_0$, where W_0 is the weight of the dry specimen and W_t is the weight of the wet specimen at time t.[52]

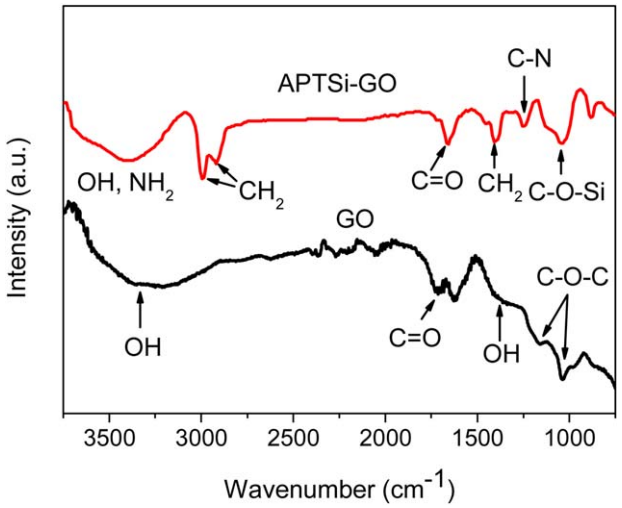

Figure 1. FT-IR spectra of GO and APTSi-GO. [Color figure can be viewed in the online issue, which is available at wileyonlinelibrary.com.]

RESULTS AND DISCUSSION

Structures and Morphologies of APTSi-GO

The preparation of APTSi-GO and FGNS/PI is shown in Scheme 1. The nucleophilic substitution reactions of the primary amine groups of APTSi with the epoxide or carboxyl groups of GO occurred by refluxing. The FT-IR spectra of GO and APTSi-GO are shown in Figure 1. The typical peaks of GO at 1711 and 1391 cm^{-1} can be attributed to the C═O and C—OH stretching vibrations of carboxyl groups, respectively. The broad peak at 3000–3600 cm^{-1} can be assigned to the OH groups. Moreover, the peaks at 1036 and 1068 cm^{-1} can be ascribed to the C—O—C stretching of epoxide groups. After the reaction with APTSi, two new strong peaks at 2980 and 2920 cm^{-1} appeared, corresponding to the symmetric and asymmetric stretching vibrations of CH_2 groups of the alkyl chains in the APTSi of APTSi-GO, respectively. The peak at 1410 cm^{-1} can be attributed to the bending mode of CH_2 groups, confirming the bonding of APTSi to GO.[53] Further evidence was provided by the characteristic absorption peaks at 1253 cm^{-1} (C—N stretching of the alkyl chains) and 1047 cm^{-1} (Si—O—C stretching vibration).[54] Moreover, the broad absorption peak at 3415 cm^{-1} (overlapping of the —NH_2 and —OH stretching vibration peaks) was weakened in the spectrum of APTSi-GO compared with that of GO (only OH

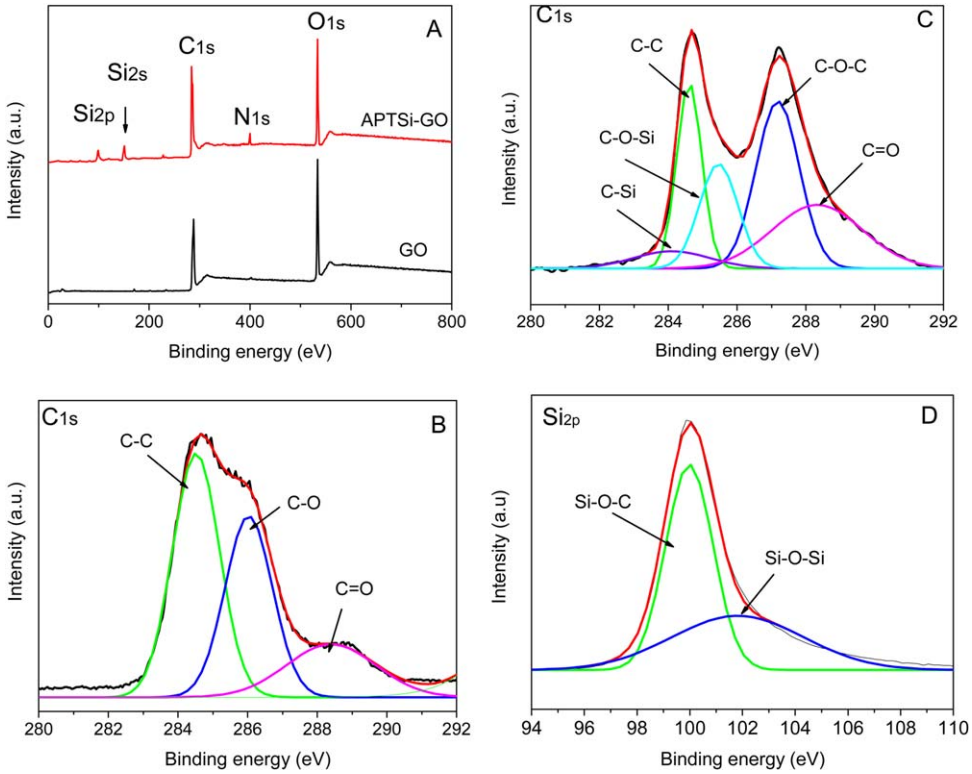

Figure 2. (A) XPS spectra of GO and APTSi-GO, (B and C) high-resolution C1s XPS of GO and APTSi-GO, respectively, and (D) high-resolution Si2p XPS spectrum of APTSi-GO. [Color figure can be viewed in the online issue, which is available at wileyonlinelibrary.com.]

stretching vibration), indicating that APTSi molecules are chemically attached to the GO surface by covalent bonding and simultaneous partial reduction of the GO nanosheets.

X-ray photoelectron spectroscopy (XPS) provides more information about the surface composition of GO and APTSi-GO, further confirming their structures. The wide-range XPS spectrum of APTSi-GO [Figure 2(A)] clearly shows three new peaks for Si2s, Si2p, and N1s, indicating successful covalent bonding of APTSi onto the surface or edge of GO nanosheets. To provide further evidence for the bonding of APTSi to GO sheets, the C1s spectra of GO and APTSi-GO were studied as shown in Figures 2(B) and (C). GO has a considerable degree of oxidation with a C/O atomic ratio of 63.8%/36.2%, and the C1s XPS spectrum of GO [Figure 2(B)] can be divided into three peaks: C—C/C=C (nonoxygenated carbon, 284.5 eV), C—O—C (epoxy, 286.6 eV), and C=O (288.5 eV). After the modification with APTSi, the XPS spectrum of C1s can be deconvoluted into five Gaussian peaks [Figure 2(C)], corresponding to the carbon atoms in different functional groups such as C—Si (284 eV), C—C, and C=C (284.6 eV), C—O—C (287.2 eV), C—O—Si (285.4 eV), and O—C=O (288.4 eV). Two new peaks are clearly

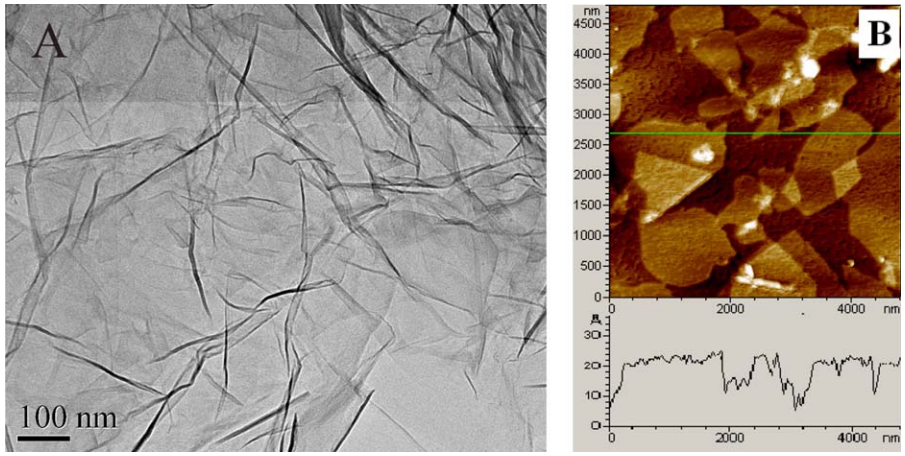

Figure 3. (A) TEM micrograph APTSi-GO nanosheets, (B) AFM image and height profile of APTSi-GO nanosheets. [Color figure can be viewed in the online issue, which is available at wileyonlinelibrary.com.]

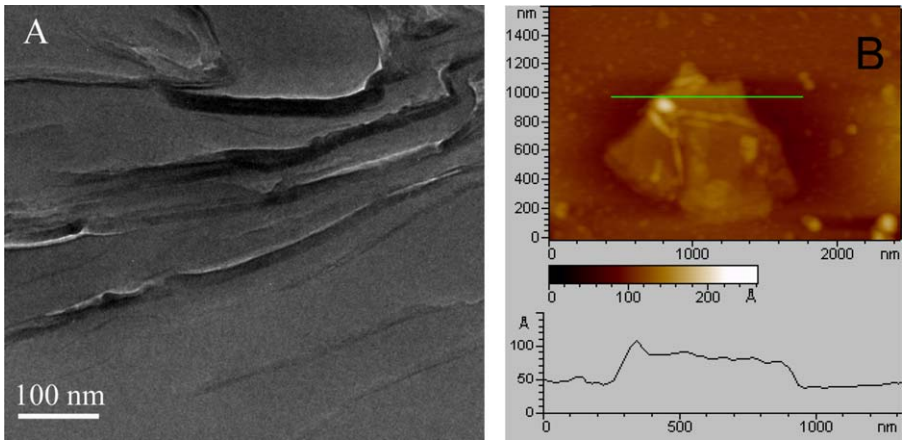

Figure 4. (A) TEM image and (B) AFM height image of 1.5% FGNS/PI. [Color figure can be viewed in the online issue, which is available at wileyonlinelibrary.com.]

observed at 284 and 285.4 eV corresponding to the signals of C—Si and C—O—Si,[55] indicating that APTSi was covalently grafted onto the GO sheets. The Si2p spectrum of APTSi-GO is shown in Figure 2(D). The peak at a bonding energy of 100 eV can be attributed to the bonding of silicon with the OH group of GO (Si—O—C), whereas the peak at 102 eV can be attributed to the siloxane (—Si—O—Si—) group resulting from the partial hydrolysis of silane molecules during the silylation reaction.[56] These results are consistent with those obtained from the FTIR studies.

The AFM and TEM images show the dispersion and exfoliation states of APTSi-GO in DMAc. The TEM micrograph of APTSi-GO is shown in Figure 3(A). Flattened nanosheets are randomly stacked together, showing transparent and rippled silk wave structure similar to GO (Figure S1, Supporting Information, Figure S1). The clearly observed wrinkles are probably caused by the grafting functionalization of APTSi and the resulting defects. The AFM samples were prepared by dropping APTSi-GO dispersed in DMAc onto freshly exfoliated mica and drying at room temperature. The AFM image shows that the APTSi-GO sheets are planar with an average thickness of ca. 1.2 nm [Figure 3(B)]. The APTSi-GO nanoplatelets are slightly thicker than those of GO (~0.8 nm, Supporting Information Figures S1 and S2), which can be probably attributed to the functionalized APTSi units grafted on the graphene nanosheets.

Morphological Study of PI-FGNS Nanocomposites

The homogeneous dispersion of nanofillers in polymeric matrices plays an important role in fabricating high-performance composites. Figure S3 shows the photographs of the pure PI and obtained composite films. With the increase in the FGNS content, the color of the composite films became darker compared with the yellow pure PI film. Furthermore, all the FGNS/PI films show homogeneous appearance by visual inspection, indicating the uniform dispersion of FGNS in the PI matrix. Thus, PI molecular chains were successfully grafted onto the surface of graphene.

The dispersion of FGNS in PI matrix was also investigated by TEM. The TEM image [Figure 4(A)] of the microtomed cross-sections of the PI composites with a 1.5 wt % FGNS loading shows a well-exfoliated and fine dispersion without any agglomerates. This can be attributed to the strong interfacial adhesion and good compatibility between APTSi-GO sheets and PAA during the *in situ* polymerization, as well as the high dispersion of FGNS after the imidization. AFM measurements were carried out to further confirm the uniform grafting of PI chain on the surface or edge of graphene sheets. Figure 4(B) shows the tapping-mode AFM image of PI-based FGNS. The PI chains grafted on the FGNS have a height of ~5 nm, compared with the thickness of GO (~0.8 nm) and APTSi-GO (~1.2 nm) shown in Supporting Information Figures S2 and 3(B), respectively. Furthermore, the polymer matrix covers the entire plane of nanofillers, indicating the homogeneous dispersion and good compatibility of FGNS in PI matrix with the present grafting approach.

The XRD patterns of graphite, GO, APTSi-GO, pure PI, and PI/FGNS composite films with various FGNS loadings are shown in Figure 5. The XRD pattern of graphite platelets shows an

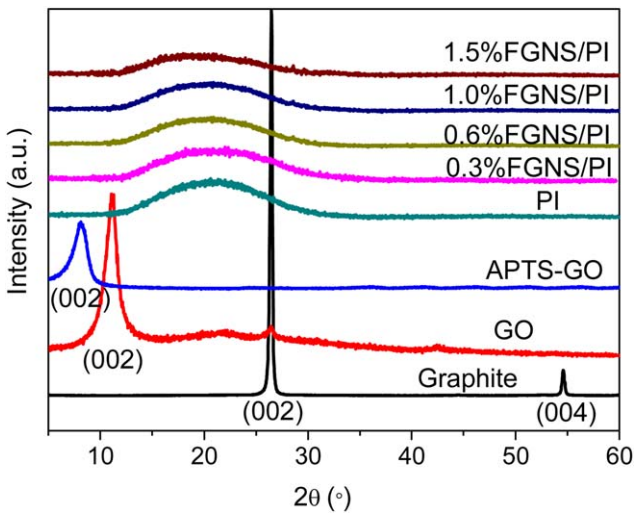

Figure 5. XRD patterns of graphite, GO, APTSi-GO, neat PI, and PI-based composite films. [Color figure can be viewed in the online issue, which is available at wileyonlinelibrary.com.]

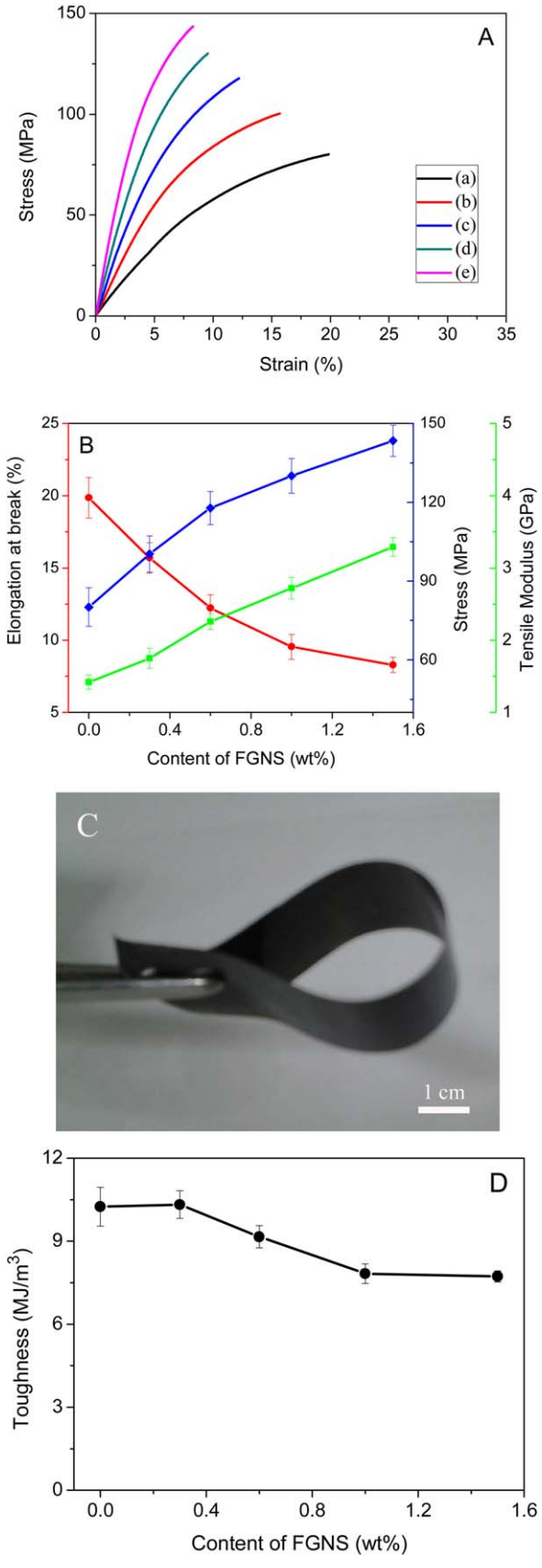

intense diffraction peak at $2\theta = 26.5°$, indicating an interlayer spacing of 0.34 nm between the platelets. After the chemical oxidation, the XRD pattern of GO shows a sharp diffraction peak centered at 11.2° corresponding to the C (002) face, and the interlayer spacing calculated from the Bragg equation was 0.8 nm. This is consistent with the AFM result (Supporting Information Figure S2), indicating the complete exfoliation of graphite into the single-layered GO. After the modification with APTSi, the diffraction peaks assigned to the interlayer distance significantly shifted to a smaller angle region at 8.07° (corresponding to the interlayer spacing of ~1.1 nm) compared with that of GO, indicating that APTSi successfully inserted into the GO interlayer via chemical bonding. This result is consistent with that of AFM [Figure 4(B)]. However, only a broad XRD peak for the PI-based composite films at ~20° was observed. The XRD results show that the stacking and regular structure of APTSi-GO disappeared, further confirming the complete exfoliation of FGNS in PI matrix. Moreover, a broad XRD peak can be attributed to the amorphous feature of the cross-linked polymer matrix. These results indicate that disordered FGNS are dispersed in the polymer matrix.

Mechanical Properties

Defect-free graphene is the strongest material ever reported with a Young's modulus of 1.1 TPa and an ultimate strength of 130 GPa.[15] Even with some structural distortion of chemical reduced graphene sheets (CMG), the elastic modulus of CMG is still as high as 0.25 TPa. The incorporation of graphene by the covalent bonding of graphene with PI at the interface and the homogeneous dispersion of graphene in the PI matrix are effective approaches to enhance the mechanical properties of PI-based composites.[56] The typical stress–strain curves of the pure PI and PI/FGNS composite films with various loadings of fillers are illustrated in Figure 6(A), and the change in the mechanical properties with various FGNS contents is shown in Figure 6(B). Clearly, the composites showed higher tensile strength and modulus compared with pure PI. Moreover, both the stress and modulus of FGNS/PI composites increased with increasing loading of FGNS. Compared with that of pure PI, the modulus and stress of 1.5% FGNS/PI composite film sharply increased by 132% from 1.42 to 3.29 GPa and 79% from 80.11 to 143.43 MPa, respectively. Such an interesting reinforcement can be mainly attributed to two aspects: (1) The strong interfacial adhesion between the FGNS and PI matrix. The amino groups of APTSi (organosiloxane with active end-group) grafted to the surface of GO can react with BPDA to form PAA and generate many strong covalent bonds between the nanofillers and PAA. After the imidization, the load may be transferred successfully from the PI matrix to the FGNS in the composites. (2) Good

Figure 6. (A) Typical stress–strain curves of pure PI (a) and PI/FGNS composite films containing (b) 0.3 wt %, (c) 0.6 wt %, (d) 1.0 wt %, and (e) 1.5 wt % of FGNS loadings. (B) Relationships of stress (blue line), tensile modulus (green line), and elongation-at-break (red line) with various FGNS contents. (C) A typical image of the 1.5 wt % FGNS/PI composite film. (D) Effect of FGNS loading content on toughness. [Color figure can be viewed in the online issue, which is available at wileyonlinelibrary.com.]

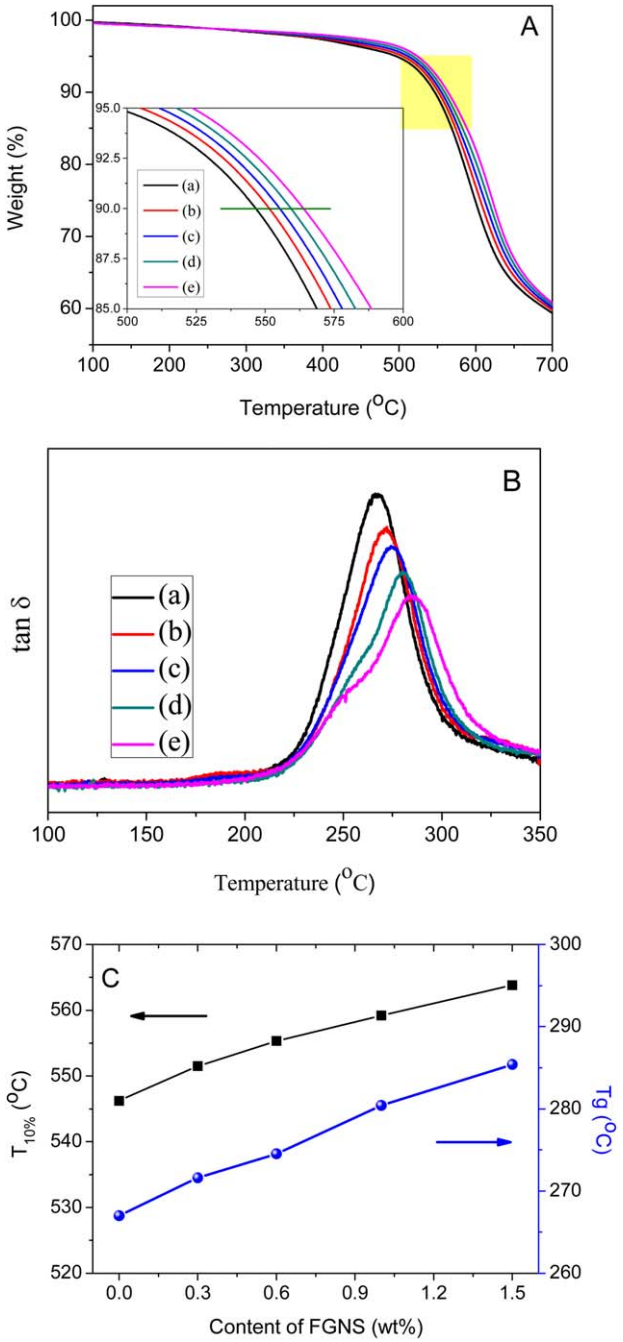

Figure 7. (A) TGA curves of (a) pure PI and PI/FGNS composite films containing (b) 0.3 wt %, (c) 0.6 wt %, (d) 1.0 wt %, and (e) 1.5 wt % of FGNS loadings at a heating rate of 10°C/min. Inset: high magnification of the light yellow section. (B) Damping spectra of pure PI and FGNS/PI nanocomposites obtained from the DMA measurements on the membranes. (C) Relationship of T_g and $T_{10\%}$ (the decomposition temperature at 10% weight loss) with content of FGNS. [Color figure can be viewed in the online issue, which is available at wileyonlinelibrary.com.]

compatibility between the FGNS and PI matrix. The well-dispersed state of the fillers in the PI matrix was formed because the grafted organic molecules, organosiloxane chains, on the GO surface can prevent their stacking and aggregation. However, the value of the elongation at break decreased with increasing FGNS loading from 19.86% (pure PI film) to 8.29% (1.5% FGNS/PI composite). This is because the FGNS within the PI matrix and the strong PI-FGNS interfacial interaction hindered the free movement of the PI chains during the extension. Fortunately, the resulting FGNS/PI composite films still retain flexibility as shown in Figure 6(C). The typical photographic image illustrates that the incorporation of a small amount of FGNS did not deteriorate the flexibility of the resultant composite films.

To reveal the phenomenon that the composite films possess flexibility, the toughness was calculated from the area under the stress–strain curve. It is quite attractive that the toughness improved a little from 10.25 to 10.32 MJ/m^3 with adding 0.3 wt % FGNS [Figure 6(D)]. The toughness then decreased to 7.73 MJ/m^3 with increasing FGNS loading to 1.5 wt %. The excellent flexibility and toughness are attributed to the strong covalent bonding to the polymer matrix which can effectively retard crack propagation during deformation.[57,58]

Thermal Properties

Thermal stability is one of the most important parameters for PI-based composite materials in high-performance engineering plastics application. Figure 7(A) shows the TGA curves of pure PI and its composites with different FGNS loadings. All the films possess excellent thermal stability. The decomposition temperature of 10% weight loss ($T_{10\%}$) gradually shifted to a higher temperature with increasing FGNS fraction as shown in the inset of Figure 7(A) and (C). Upon the incorporation of 1.5 wt % FGNS, the $T_{10\%}$ increased by 18°C compared with that of the pure PI film (546°C). This can be attributed to the uniform dispersion of FGNS and strong covalent adhesion between the fillers and polymer matrix.

Figure 7(B) shows the results of typical damping spectra and the corresponding glass-transition temperatures (T_g) of the pure PI and PI-based composites with various FGNS loadings. The tanδ peaks broaden and the peak heights decreased with increasing FGNS loadings. Moreover, the T_g of the FGNS/PI composites displays an obvious increasing trend with increasing the content of FGNS. The PI with 1.5 wt % FGNS has an 18.4°C higher T_g than that of the pure PI ($T_g = 267$°C) as illustrated in Figure 7(C). The increased T_g of the composites was due to the existence of covalent bonding at the FGNS/PI interfaces and the efficient dispersion of FGNS in the nanocomposites, which caused the restricted segmental motions at the polymer chain and FGNS fillers interface. As a result of restriction effect, natural segmental motion and relaxation can only occur at higher temperatures and over a broader temperature range,[59] proving the two main features observed above.

The excellent thermal conductivity of pristine graphene encourages us to investigate the effect of the resultant FGNS/PI nanocomposites. Figure 8 shows that the thermal conductivity of neat PI and its nanocomposites with various FGNS loadings. With increasing FGNS concentration, thermal conductivity displays a clear increasing trend. Upon the incorporation of 1.5 wt % FGNS, the thermal conductivity value became double than that of the neat PI film (0.165 W/m·K). This significant improvement can be ascribed to the excellent thermal

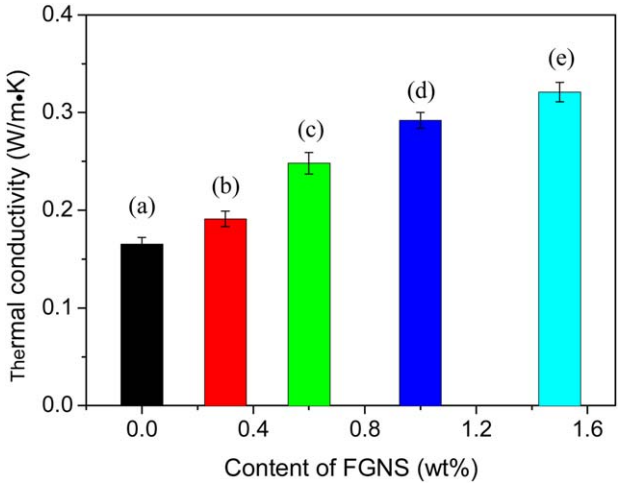

Figure 8. Thermal conductivity of pure PI films and FGNS/PI films. [Color figure can be viewed in the online issue, which is available at wileyonlinelibrary.com.]

conductivity of FGNS and the formation of a conducting network due to the chemical covalent adhesion and homogeneous dispersion in the composites.

Electrical Conductivity and Water Absorption Properties

Single-layer graphene has a very high electrical conductivity up to 6000 S/cm,[26] therefore it can improve the electrical conductivity of the resultant composites. Large-scale graphene-based composites have been demonstrated for industrial applications with reasonable cost and productivity,[60] such as high barrier and gas sensing properties,[61] amplified colorimetric sensors for target DNA detection,[62,63] glucose detection,[64] energy conversion/storage,[65] high performance, and flexible electromagnetic shielding nanocomposites.[66]

Figure 9 shows that the electrical conductivity of the FGNS/PI composites sharply increased with increasing filler content. The electrical conductivity of the pure PI, graphite, the derivatives of graphite, and PI-based composites are listed in Table I. Upon the addition of 1.5 wt % FGNS, the conductivity increased

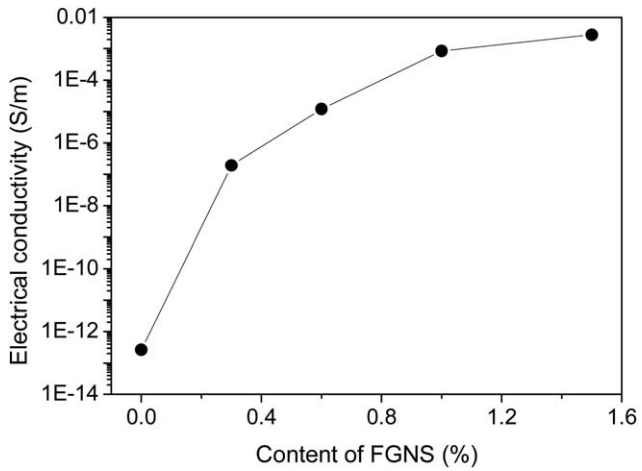

Figure 9. Electrical conductivity of pure PI and FGNS/PI films.

Table I. Data of Electrical Conductivity, Water Uptake of Pure PI, and FGNS/PI Composites

Samples	Electrical conductivity (S/m)	Water uptake (wt %)
Pure PI film	2.6×10^{-13}	2.82
0.3% FGNS-PI	1.9×10^{-7}	2.31
0.6% FGNS-PI	1.2×10^{-5}	1.97
1.0% FGNS-PI	8.6×10^{-4}	1.53
1.5% FGNS-PI	2.8×10^{-3}	1.29
[56]CRGO	3.2×10^{3}	-
[56]ERGO	3.5×10^{3}	-
This work FGNS	5.6×10^{3}	-

remarkably from 2.6×10^{-13} to 2.8×10^{-3} S/m (Table I) which is 10 orders of magnitude higher than that of pure PI. This might be attributed to the higher electrical conductivity of FGNS (5.6×10^{3} S/m) and the formation of a conductive network through the PI matrix. In this study, it is found that the FGNS conductivity is higher than those of chemical reduced graphene oxide (CRGO) and electrochemical reduced graphene oxide (ERGO).[67] When the FGNS content is over 1.0 wt %, the conductivity improved smoothly with increasing filler content. Luong *et al.*[30] achieved an electrical conductivity of 8.9×10^{-5} S/m by the incorporation of 0.75 wt % functionalized graphene sheets into PI. However, a much higher electrical conductivity of 1.6×10^{-4} S/m by the addition of 0.6 wt % FGNS was achieved in the present study. This can be attributed to the uniform dispersion of FGNS and strong covalent adhesion between the fillers and polymer matrix during *in situ* polymerization, which will be propitious to loose network formation and effective conductive improvement compared with that of pure PI.

In general, PI with low water absorption is in urgent need for advanced microelectronic devices. All the samples show low water uptake as shown in Table I. With increasing FGNS content from 0 to 1.5%, the water uptake of the FGNS/PI composites decreased from 2.82 to 1.29%. This phenomenon may be related to the increase in hydrophobicity caused by adding FGNS via covalent bonding.

CONCLUSION

We developed, for the first time, a facile and effective approach to prepare high-performance PI-based nanocomposites via *in situ* polymerization and thermal imidization. The APTSi-GO exhibited good dispersion and compatibility with the polymer matrix due to the strong interfacial covalent interaction. The FGNS/PI composites show a 79% improvement in the tensile strength and a 132% increase in the tensile modulus by adding 1.5 wt % of FGNS, indicating the efficient load transfer between the reinforcing fillers and PI matrix. Moreover, the thermal stability and T_g of the PI/FGNS composites are effectively improved by taking the advantages of the unique properties of FGNS. Notably, the electrical and thermal conductivities of the composites are significantly improved by adding 1.5 wt % of FGNS, which are $\sim 10^{10}$ and two times higher than those of

pure PI, respectively. The success of this approach has great application potential in graphene-based polymer nanocomposites, especially in multifunctional and high-performance PI-based composite materials.

ACKNOWLEDGMENTS

This work was supported by the National Natural Science Foundation of China (No. 21264001, 21004009), Natural Science Foundation of Jiangxi Province (No. 20114BAB213010), Young Scientist Foundation of Jiangxi Province (No. 20133BCB23020), and Foundation of Jiangxi Educational Committee (No. GJJ14471, GJJ13447).

REFERENCES

1. Huang, J. C. *Adv. Polym. Technol.* **2002**, *21*, 299.
2. Chen, Q.; Wu, W. D.; Zhao, Y.; Xi, M.; Xu, T.; Fong, H. *Compos. Part B* **2014**, *58*, 43.
3. Li, M. C.; Zhang, Y.; Cho, U. R. *Mater. Des.* **2014**, *63*, 565.
4. Moniruzzaman, M.; Winey, K. I. *Macromolecules* **2006**, *39*, 5194.
5. Zhang, B.; Zang, W.; Tian, Y.; Zhang, K.; Chen, C. *J. Appl. Polym. Sci.* **2014**, *131*, 40479.
6. Li, M. C.; Deng, X.; Cho, U. R. *J. Compos. Mater.* **2010**, *44*, 1279.
7. Calleja, F. J. B.; Girl, L.; Asano, T.; Mieno, T.; Sakurai, A.; Ohnuma, M.; Sawatari, C. *J. Mater. Sci.* **1996**, *31*, 5153.
8. Wang, D. H.; Tan, L. S.; Huang, H. J.; Dai, L. M. *Macromolecules* **2009**, *42*, 114.
9. Li, M. C.; Cho,U. R. *Mater. Lett.* **2013**, *92*, 132.
10. Li, M. C.; Ge, X.; Cho, U. R. *Macromol. Res.* **2013**, *21*, 519.
11. Stankovich, S.; Dikin, D. A.; Dommett, G. H. B.; Kohlhaas, K. M.; Zimney, E. J.; Stach, E. A.; Pinen, R. D.; Nguyen, S. T.; Ruoff, R. S. *Nature* **2006**, *442*, 282.
12. Novoselov, K. S; Geim, A. K.; Morozov, S. V.; Jiang, D.; Zhang, Y.; Dubonos, S. V.; Grigorieva, I. V.; Firsov, A. A. *Science* **2004**, *306*, 666.
13. Lee, C.; Wei, X.; Kysar, J. W.; Hone, J. *Science* **2008**, *321*, 385.
14. Du, X.; Skachko, I.; Barker, A.; Andrei, E. Y. *Nat. Nanotechnol.* **2008**, *3*, 491.
15. Kim, H.; Abdala, A. A.; Macosko, C. W. *Macromolecules* **2010**, *43*, 6515.
16. Balandin, A. A.; Ghosh, S.; Bao, W.; Calizo, I.; Teweldebrhan, D.; Miao, F.; Lau, C. N. *Nano Lett.* **2008**, *8*, 902.
17. Li, X. S.; Cai, W. W.; An, J. H.; Kim, S.; Nah, J.; Yang, D. X.; Piner, R.; Velamakanni, A.; Jung, I.; Tutuc, E.; Banerjee, S. K.; Colombo, L.; Ruoff, R. S. *Science* **2009**, *324*, 1312.
18. Wang, H. L.; Cui, L. F.; Yang, Y.; Casalongue, H. S.; Robinson, J. T.; Liang, Y. Y.; Cui, Y.; Dai, H. J. *J. Am. Chem. Soc.* **2010**, *132*, 13978.
19. Sun, X. M.; Liu, Z.; Welsher, K.; Robinson, J. T.; Goodwin, A.; Zaric, S.; Dai, H. *J. Nano Res.* **2008**, *1*, 203.
20. Liu, Z.; Robinson, J. T.; Sun, X. M.; Dai, H. J. *J. Am. Chem. Soc.* **2008**, *130*, 10876.
21. Lu, C. H.; Yang, H. H.; Zhu, C. L.; Chen, X.; Chen, G. N. *Angew. Chem. Int. Ed.* **2009**, *48*, 4785.
22. Chen, S.; Zhu, J. W.; Wu, X. D.; Han, Q. F.; Wang, X. *ACS Nano* **2010**, *4*, 2822.
23. Chandra, V.; Park, J.; Chun, Y.; Lee, J. W.; Hwang, I. C.; Kim, K. S. *ACS Nano* **2010**, *4*, 3979.
24. Zhang, H. W.; Zhou, L.; Yu, C. Z. *RSC Adv.* **2014**, *4*, 495.
25. Park, O. K.; Hwang, J. Y.; Goh, M.; Lee, J. H.; Ku, B. C.; You, N. H. *Macromolecules* **2013**, *46*, 3505.
26. Hu, K.; Kulkarni, D. D.; Choi, I.; Tsukruk, V. V. *Prog. Polym. Sci.* **2014**, *39* 1934.
27. Shi, H.; Li, Y.; Guo, T. *J. Appl. Polym. Sci.* **2013**, *128*, 3163
28. Kuilla, T.; Bhadra, S.; Yao, D.; Kim, N. H.; Bose, S.; Lee, J. H. *Prog. Polym. Sci.* **2010**, *35*, 1350.
29. Potts, J. R.; Dreyer, D. R.; Bielawski, C. W.; Ruoff, R. S. *Polymer* **2011**,*52*, 5.
30. Luong, N. D.; Hippi, U.; Korhonen, J. T.; Soininen, A. J.; Ruokolainen, J.; Johansson, L. S.; Do Nam, J.; Sinh, L. H.; Seppälä, J. *Polymer* **2011**, *52*, 5237.
31. Wang, G. X.; Wang, B.; Park, J.; Yang, J. A.; Shen, X. P.; Yao, J. *Carbon* **2009**, *47*, 68.
32. Lin, Z. Y.; Liu, Y.; Wong, C. P. *Langmuir* **2010**, *26*, 16110.
33. Li, W. J.; Tang, X. Z.; Zhang, H. B.; Jiang, Z. G.; Yu, Z. Z.; Du, X. S.; Mai, Y. W. *Carbon* **2011**, *49*, 4724.
34. Ma, W. S.; Li, J.; Deng, B. J.; Zhao, X. S. *J. Mater. Sci.* **2013**, *48*, 156.
35. Ma, W. S.; Wu, L.; Yang, F.; Wang, S. F. *J. Mater. Sci.* **2014**, *49*, 562.
36. Yang, H. F.; Shan, C. S.; Li, F. h.; Han, D. G.; Zhang, Q. X.; Niu, L. *Chem. Commun.* **2009**, *26*, 3880.
37. Compton, O. C.; Dikin, D. A.; Putz, K. W.; Brinson, L. C.; Nguyen, S. T. *Adv. Mater.* **2010**, *22*, 892.
38. Fang, M.; Wang, K. Q.; Lu, H. B.; Yang, Y. L.; Nutt, S. *J. Mater. Chem.* **2009**, *19*, 7098.
39. Yang, H. F.; Yang, H. F.; Li, F. H.; Shan, C. S.; Han, D. G.; Zhang, Q. X.; Niu, L.; Ivaska, A. *J. Mater. Chem.* **2009**, *19*, 4632.
40. Fang, M.; Wang, K. G.; Lu, H. B.; Yang, Y. L.; Nutt, S. *J. Mater. Chem.* **2010**, *10*, 1982.
41. Yoonessi, M.; Shi, Y.; Scheiman, D. A.; Marisabel, L. C.; Tigelaar, D. M.; Weiss, R. A.; Meador, M. A. *ACS Nano* **2012**, *6*, 7644.
42. Chung, I. S.; Park, C. E.; Ree, M.; Kim, S. Y. *Chem. Mater.* **2001**, *13*, 2801.
43. Ha, H. W.; Choudhury, A.; Kamal, T.; Kim, D. H.; Park, S. Y. *ACS Appl. Mater.* **2012**, *4*, 4623.
44. Zhang, Y.; Xiao, S.; Wang, Q.; Liu, S.; Qiao, Z.; Chi, Z.; Xu, J. *J. Mater. Chem.* **2011**, *21*, 14563.
45. Yuan, W.; Che, J. J.; Mary, B, C. P. *Chem. Mater.* **2011**, *23*, 4149.
46. Chen, D.; Zhu, H.; Liu, T. *ACS Appl. Mater.* **2010**, *2*, 3702.
47. Liu, H.; Li, Y.; Wang, T.; Wang, Q. *J. Mater. Sci.* **2012**, *47*, 1867.

48. Huang, T.; Lu, R.; Su, C.; Wang, H.; Guo, Z.; Liu, P.; Huang, Z.; Chen, H.; Li, T. *ACS Appl. Mater.* **2012**, *4*, 2699.
49. Kovtyukhova, N. I.; Ollivier, P. J.; Martin, B. R.; Mallouk, T. E.; Chizhik, S. A.; Buzaneva, E. V.; Gorchinskiy, A. D. *Chem. Mater.* **1999**, *11*, 771.
50. Qian, Y.; Wang, C. Y. *Appl. Surf. Sci.* **2011**, *257*, 10758.
51. Veca, L. M.; Meziani, M. J.; Wang, W.; Lu, F.; Zhang, P.; Connell, J. W.; Sun, Y. P. *Adv. Mater.* **2009**, *21*, 2088.
52. Li, M. C.; Ge, X.; Cho, U. R. *Macromol. Res.* **2013**, *21*, 793.
53. Tao, L. L.; Zhou, B.; Bai, G. X.; Wang, Y. G.; Yu, S. F.; Lau, S. P.; Tsang, Y. H.; Yao, J. Q.; Xu, D. G. *J. Phys. Chem. C* **2013**, *117*, 23108.
54. Ou, J. F.; Wang, J. Q.; Liu, S.; Mu, B.; Ren, J. F.; Wang, H. G.; Yang, S. G. *Langmuir* **2010**, *20*, 15830.
55. Das, A.; Pisana, S.; Chakraborty, B.; Piscanec, S.; Saha, S. K.; Waghmare, U. V.; Novoselov, K. S.; Krishnamurthy, H. R.; Geim, A. K.; Ferrari, A. C. *Nat. Nanotechnol.* **2008**, *3*, 210.
56. Park, O. K.; Lee, S.; Joh, H. I.; Kim, J. K.; Kang, P. H.; Ku, B. C. *Polymer* **2012**, *53*, 2168.
57. Che, J. F.; Chan-Park, M. B. *Adv. Funct. Mater.* **2008**, *18*, 888.
58. Pan, Y.; Xu, Y.; An, L.; Lu, H.; Yang, Y.; Chen, W.; Nutt, S. *Macromolecules* **2008**, *41*, 9245.
59. Chen, Z. X.; Lu, H. B. *J. Mater. Chem.* **2012**, *22*, 12479.
60. Wang, J.; Liang, M.; Fang, Y.; Qiu, T.; Zhang, J.; Zhi, L. *Adv. Mater.* **2012**, *24*, 2874.
61. Llobet, E. *Sens. Actuators B* **2013**, *179*, 32.
62. Xing, X. J.; Liu, X. G.; He, Y.; Lin, Y.; Zhang, C. L; Tang, H. W.; Pang, D. W. *Biomacromolecules* **2012**, *14*, 117.
63. Wang, Y.; Wu, Z.; Liu, Z. *Anal. Chem.* **2012**, *85*, 258.
64. Qiu, J. D.; Shi, L.; Liang, R. P.; Wang, G. C.; Xia, X. H. *Chem. Eur. J.* **2012**, *18*, 7950.
65. Sun, H.; Xu, Z.; Gao, C. *Adv. Mater.* **2013**, *25*, 2554.
66. Secor, E. B.; Prabhumirashi, P. L.; Puntambekar, K.; Geier, M. L.; Hersam, M. C. *J. Phys. Chem. Lett.* **2013**, *4*, 1347.
67. Guo, H. L.; Wang, X. F.; Qian, Q. Y.; Wang, F. B.; Xia, X. H. *ACS Nano* **2009**, *3*, 2653.